Fouling Resistant 2D Boron Nitride Nanosheet – PES Nanofiltration Membranes

Ze-Xian Low,[1] Jing Ji,[2] David Blumenstock,[2] Yong-Min Chew,[2] Daniel Wolverson,[3] and Davide Mattia*[2]

[1]Department of Chemical Engineering, Monash University, Clayton, VIC 3800, Australia
[2]Centre for Advanced Separations Engineering and Department of Chemical Engineering, University of Bath, Claverton Down, Bath BA2 7AY, UK.
[3]Centre for Nanoscience and Nanotechnology and Department of Physics, University of Bath, Claverton Down, Bath BA2 7AY, UK.

Corresponding author: d.mattia@bath.ac.uk, phone: +44-(0)1225-383961

Abstract:

A novel fouling-resistant nanofiltration mixed-matrix membrane was obtained by the incorporation of 2D boron nitride nanosheets (BNNS) in polyethersulfone (PES). The addition of just 0.05 wt% of BNNS into the PES matrix led to a 4-fold increase in pure water permeance with a 10% decrease in the rejection of the dye Rose Bengal; up to 95% rejection of humic acid and nearly 100% flux recovery over two cycles in cross-flow fouling tests without the need for chemical cleansing. This performance is attributed to the uniform distribution of the BNNS in the PES matrix, observed via Raman mapping, and the surface chemistry and structure of the BNNS, which hydrophilised the polymer matrix and reduced its surface roughness. The low amount of BNNS filler needed to render the mixed-matrix membrane fouling-resistant opens the way to its use in waste-water treatment applications where organic fouling remains a major challenge.

keywords: boron nitride nanosheets; PES; fouling; nanofiltration

1. Introduction

As demand for clean water increases due to a growing population and depleting fresh water sources, much academic research has been focused on developing novel membrane materials with ever higher permeance (volume of water permeating the membrane per unit of time, surface and applied pressure). While a higher permeance could reduce the overall size of a membrane-based water treatment plant, most of the running costs of such plants are associated with fouling. This is the accumulation of rejected matter on the feed side or within a membrane, which causes significant reductions in permeance and can, eventually, stop all flow through the membrane itself. Polymeric membranes, which occupy the vast majority of the market for water treatment, suffer significantly from fouling. As such, one of the main strategies explored to address this problem has been the development of mixed matrix membranes (MMMs), where a second, often inorganic, phase is added to modify the surface properties of the polymer matrix to reduce fouling deposition. Amongst the wide range of nanomaterials tested, 2D nanomaterials, with their promising physico-chemical properties, have rapidly become heavily investigated as fillers for mixed-matrix applications. These include graphene [1] and its derivatives (GO and rGO) [2], graphitic carbon nitride [3, 4], and many others [5].

Hexagonal boron nitride (*h*-BN) is the most stable form among BN polymorphs [6], structurally analogous to graphene, with high chemical (in a wide range of acids and alkalis) and temperature (up to 900 °C) stability, low density, high thermal conductivity, electrical insulation, and low coefficient of friction [7]. *h*-BN can be formed in 0D, 1D and 2D structures through a variety of fabrication techniques [7, 8]. In particular, 2D structures, called boron nitride nanosheets (BNNS), have sp^2 hybridized B-N bonds, a high surface area and numerous structural defects which become anchoring points for functionalisation [7, 9] .These BNNS can be produced via thermal decomposition [7], chemical blowing [10], and exfoliation [11]. The latter is the preferred method for the production of controlled few-layer BNNS structures, though the properties of the exfoliated BNNS are highly dependent on the exfoliation method used, particularly the choice of solvents and length of ultra-sonication [11]. Exfoliation methods present in the literature have primarily focused on producing single- or few-layer structures [12]. involving long sonication times [13], and at the expense of lateral size and yield [14], and leading to the creation of numerous defects [11-14]. The need for longer sonication times can be attributed to the strong partially-ionic interlayer interaction between BN layers, compared to the weaker Van der Waals one between graphene layers [15] .

The attractive properties of BN nanomaterials have led to significant investigation into their use as sorbents for the removal of pollutants from water [16], including oils [17], metal ions [18], and a wide range of dyes (e.g. methylene blue, neutral red, methyl orange, congo red and basic yellow) [19, 20]. The strong sorption capacity of BN nanostructures for organic substances is attributed to π–π stacking [16]. BNNS, in the form of powders of monoliths, have also shown to be effective at adsorbing natural organic matter [21]. one of the primary causes of membrane fouling and oils and organic solvents [20]. The use of BNNS in

membranes, in contrast, has been more limited, with BNNS added to PVDF for enhanced oil removal [22], and emulsion break-up [23]. BNNS have also been incorporated in polymers [24]. including poly(methyl methacrylate) (PMMA), polystyrene (PS) and polycarbonate (PC), to improve the thermo-conductive insulation [25] or mechanical properties [10], not filtration. To the authors' knowledge, there are no publications on the use of BNNS mixed matrix membranes for water treatment or fouling reduction.

Herein, we prepared a novel mixed matrix polyether sulfone (PES) nanofiltration membrane incorporating BNNS obtained via a novel exfoliation method based on ultra-sonication and microwave irradiation. The enhancement to the nanofiltration membrane by incorporating BNNS is remarkable, where flux enhancement and completely reversible fouling are achieved without the need for chemical cleaning. The complete fouling reversibility was confirmed by performing successive fouling and cleaning cycles on the samples.

2. Materials and Methods

2.1 Materials

Hexagonal boron nitride (*h*-BN) was purchased from UK abrasive, U.S.A. Sodium dodecyl sulfate (SDS) was purchased from Merck, U.K. N-methyl-2-pyrrolidone (NMP), Rose Bengal (Mw: 1017.64 Da) and humic acid sodium salt were purchased from Sigma-Aldrich, U.K. Poly(ethersulfone) (PES; Radel A300) was kindly provided by Prof. Kang Li (Imperial College London, U.K.). The water used for the experiments was purified with a water purification system (PURELAB Chorus 1 Complete, Veolia, U.K.) with resistivity of 18.2 MΩ/cm.

2.2 Preparation of BNNS

Hexagonal boron nitride nanosheets (BNNS) were prepared by first dispersing 5 g of *h*-BN powder and 1.5 g of SDS in 1 L of de-ionized water. The solution was then ultrasonicated (ultrasonic bath, 45 kHz, 80 W) for 1 h. The suspension was subsequently microwave irradiated at 804 W for 2 min in multiple 60 ml Teflon lined high pressure vessels (MARS Synthesis, CEM, U.K.). A total of 6 vessels were microwave irradiated per batch. The irradiated suspension was left overnight for sedimentation and centrifuged the next day at 3000 rpm for 1 h. The supernatant was collected and subsequently centrifuged at 10000 rpm for 1 h. The sediment was recovered and rinsed with deionized water. The centrifugation step was repeated twice to obtain the BNNS after which the BNNS is centrifuged twice using NMP in place of water. The final solution has the volume of about 20 ml. The concentration of BNNS in NMP was determined by gravimetric method to be 0.0156 g BNNS per 1 g of NMP.

2.3 Membrane Fabrication

The PES and PES-BNNS nanocomposite membranes were prepared via non-solvent induced phase separation at room temperature. Three different concentrations of BNNS (0.025 wt%, 0.05 wt% and 0.1 wt%) were used in this study. For instance, to prepare the PES casting

solution with 0.025 wt% BNNS, 1.12 g of BNNS-NMP suspension (based on the calculation of the concentration of BNNS in NMP) were first added into 52.61 g of NMP and stirred for 15 min. 16.05 g of PES was then added, and the solution was stirred overnight until the PES was completely dissolved. The solution was left to degas for 8 h before use. **Table 1** shows the composition of the casting solutions.

Table 1. Composition of the casting solutions for PES and PBNS nanocomposite membranes.

Membrane	PES (wt%)	NMP (wt%)	BNNS (wt%)
PES-pure	23.000	77.000	0.000
PBNS0.025	23.000	76.975	0.025
PBNS0.05	23.000	76.950	0.050
PBNS0.1	23.000	76.900	0.100

The membranes were cast on a glass plate using an automated film applicator with stainless steel blade at a gap of 200 µm (Elcometer, U. K.) at room temperature. The non-solvent induced phase inversion step was performed by immersing the membrane in a coagulation bath of de-ionized water for at least 24 h. The membranes were subsequently removed from the bath and stored in fresh deionized water for later use. 0.025 wt%, 0.05 wt%, and 0.1 wt% PES-BNNS nanocomposite membranes were denoted as PBNS0.025, PBNS0.05 and PBNS0.1, respectively.

2.4 Characterization of BNNS

The phase of BNNS was determined using powder X-ray diffraction (40 mA and 40 kV) at a step size of 0.02° (PXRD; BRUKER D8-Advance, Cu Kα1 radiation, USA). High resolution transmission electron microscopy (HRTEM) images and selected-area electron diffraction (SAED) were obtained using a transmission electron microscope (TEM; JEOL JEM-2100Plus, Japan). Energy-dispersive X-ray spectroscopy (EDS) and mapping were obtained using an EDS detector (Oxford Instruments X-Max detector, U.K.) attached to the TEM. Fourier transform infrared spectroscopy (FT-IR) was performed using Frontier FT-IR spectrometer, PerkinElmer. Raman Spectroscopy was performed using a Renishaw RM1000 Raman microscope using a frequency-doubled argon ion laser (244 nm, 5.08 eV) with a 40× UV objective. The thickness of the BNNS was determined using atomic force microscopy (AFM; Nanosurf EasyScan 2 Flex, Switzerland).

2.5 Membrane Characterisation

The viscosity of the solution was measured at 25 °C using a rotational rheometer (C-VOR, Bohlin Instruments, U.K.). A shear rate in the range of 0.07 to 8.88 s^{-1} was used, and the average of five measurements for each shear rate is reported for each sample (Fig. S1).

Membrane cross-sectional images were obtained using JEOL SEM6480LV, Japan. Membrane samples were prepared by drying at room temperature and sputter-coating with a 2 nm thickness of gold (Edwards Sputter Coater S150B, Mechatech Systems, UK). For imaging the cross section, the membrane was fractured in liquid nitrogen to retain its structure. The morphologies of the samples were examined using atomic force microscopy (AFM; Nanosurf EasyScan 2 Flex, Switzerland). The samples were taped onto a glass slide and scanned in tapping mode (scan size of 5 µm, time/line of 1 s, samples/line of 256) with a monolithic silicon AFM probe (Tap190Al-G, BudgetSensors, Bulgaria; spring constant: 48 N/m, resonant frequency: 190 kHz, a nominal tip radius: < 10 nm).

Raman mapping of membrane cross-sections were performed using a Raman microscope (RM1000, Renishaw, U.K.) using a frequency-doubled argon ion laser (244 nm, 5.08 eV) with a 40× UV objective lens. PBNS0.1 was used as the example to show distribution of BNNS in the membrane cross-section. Four regions of membrane cross-sections were mapped to provide statistically representative information for the distribution of BNNS in the membrane. The whole membrane cross-sections were divided to four regions as the cross-section of the membrane obtained from snapping in liquid nitrogen was rough. Raman mapping of membrane surfaces were performed using a Raman spectrometer (Renishaw inVia system, U.K.) using a green laser with 50× objective lens. Regions of 500 µm × 100 µm were scanned using line mapping technique with a step size of 1.3 µm. The water contact angles of the membranes surface were measured using a contact angle goniometer by the sessile drop technique (OCA15, Dataphysics, Germany). Images were taken at 1 s intervals for 10 s. An average of minimum 15 measurements was reported. To calculate the surface free energy of membranes, Owens, Wendt, Rabel and Kaelble (OWRK) method was applied [26]. In this method, contact angles for water and diiodomethane were measured. The surface free energy γ_S of the membrane was calculated using the equation below:

$$\gamma_S = \gamma_S^d + \gamma_S^p$$

where γ_S^d is the dispersion component and γ_S^p is the polar component of the overall surface free energy. The non-polar component γ_S^d can be calculated from the contact angle θ and free energies γ of water (W) and diiodomethane (Di) using the equation below:

$$\gamma_S^d = \left(\frac{\gamma_{Di}(1 + cos\theta_{Di}) - \gamma_W(1 + cos\theta_W)\sqrt{\frac{\gamma_{Di}^p}{\gamma_W^p}}}{2\left(\sqrt{\gamma_{Di}^d} - \sqrt{\frac{\gamma_{Di}^p \gamma_W^d}{\gamma_W^p}}\right)} \right)^2$$

On the other hand, the polar component γ_S^p can be calculated by

$$\gamma_S^p = \left(\frac{\gamma_W(1 + cos\theta_W) - 2\sqrt{\gamma_S^d \gamma_W^d}}{2\sqrt{\gamma_W^p}} \right)^2$$

Table S1 shows the parameters of the two liquids used in this work.

The surface zeta potential of the membranes was measured using a Malvern Zetasizer NS (U.K.). A tracer solution was prepared by adding a low concentration of polystyrene in 10mM NaCl solution (conductivity of 1139 µS/cm and pH value of 5.25). The reported zeta potential results are calculated from 3 – 4 measurements at different displacements and are displayed in Fig. S2. The pure tracer potential of −39.8 ± 3.1 mV was measured by three repeats of the solution without any samples. The surface zeta potentials of the membranes were calculated using the equation below:

$$\zeta_{\text{surface}} = -\zeta_{\text{reported}} + \zeta_{\text{tracer}}$$

where ζ_{surface} is the surface zeta potential, $-\zeta_{\text{reported}}$ is the measured zeta potential based on extrapolation to zero displacement and ζ_{tracer} is the zeta potential of the tracer.

Fourier transform infrared spectroscopy (FT-IR) was performed on pre-cut membrane sheets in ATR mode using a Frontier FT-IR spectrometer, PerkinElmer. DMA was performed to measure the dynamic mechanical properties and thermal behavior of the film (DMA1, Mettler Toledo, Switzerland). The films, with dimensions of 20 × 5 × 0.1 mm, were heated in tensile mode by heating from room temperature to 250 °C at a rate of 5 °C/min in air. The amplitude and frequency were set as 20 µm and 1 Hz, respectively. TG-EGA was performed using a thermogravimetric analyser (Setsys Evolution TGA 16/18, Setaram, France) at a heating rate of 10 °C/min in air from room temperature to 800 °C. The evolving gases are measured using a mass spectrometer, equipped with a quadrupole mass analyser and a SEM detector (Omnistar GSD 320, Pfeiffer Vacuum, Germany).

The porosity of the film was determined by gravimetric method using the equation below:

$$\rho(\%) = \frac{(W_w - W_d)/D_w}{(W_w - W_d)/D_w + (W_d/D_p)} \times 100\% \quad (1)$$

where ρ is the porosity of membrane (%), W_w is the wet sample weight (g), W_d is the dry sample weight (g), D_w is the density of water (0.998 g cm^{-3}) and D_p is the density of polymer (0.370 g cm^{-3}). The average of three samples for each membrane is reported.

2.6 Membrane performance

The concentration of Rose Bengal was determined using a UV spectrophotometer (UV Cary 100, Agilent, U.K.) based on a predetermined calibration curve (Fig. S3). 100 ml of Rose Bengal solution (M_w: 1017.64; 0.01 g/L) was used as the feed in a dead end stirred cell (HP4750 Stirred Cell, Sterlitech, USA) using various membrane cut to 50 mm diameter. 20 ml of permeate was collected. The mass balance was performed to check loss of material in the batch filtration experiment using the equation below. In all experiments, the mass balance for each solute was consistently >98%.

$$mass\ balance_i\ (\%) = \left(\frac{V_{permeate,i}C_{permeate,i} + V_{retentate,i}C_{retentate,i}}{V_{feed,i}C_{feed,i}}\right) \times 100 \qquad (2)$$

Water flux and flux recovery were measured in crossflow mode. A schematic diagram of the bench-scale flux test setup is shown in Fig. S4. The deionized water flux test was performed at 800 kPa and room temperature with an effective membrane area of 1.77×10^{-3} m^2. The membrane was pre-compacted at 1000 kPa for at least 60 min or until constant flux was reached. A fouling test was performed to determine the fouling resistance of the membranes. After complete compaction of the membranes, these were fouled by filtration of humic acid (1 wt%, pH 10) at 400 kPa for 240 min and a crossflow velocity of 170 ml/min. The change to the membrane permeance was recorded. The fouled membranes then underwent an in-place physical cleaning cycle. The membranes in the cells were washed with de-ionized water by circulating deionized water at a crossflow velocity of 660 ml/min for 60 min. After the cleaning step, the membrane permeance was measured at constant pressure of 800 kPa and at crossflow velocity of 170 ml/min. Each membrane went through 2 fouling cycles and 2 cleaning cycles. To evaluate the fouling performance of the membranes, the flux recovery (*FR*) of membranes was calculated as follows:

$$FR(\%) = \frac{J_{AF}}{J_{BF}} \times 100 \qquad (3)$$

where J_{BF} and J_{AF} are the pure water flux of the membrane before and after the fouling and cleaning, respectively. The fouling behavior was investigated by estimating the membrane total resistance (R_t):

$$R_t = R_m + R_r + R_{ir} \qquad (4)$$

where R_m is the intrinsic membrane resistance, R_{ir} is the irreversible resistance, and R_r is the reversible resistance:

$$R_m = \frac{TMP}{\mu \times J_{BF}} \qquad (5)$$

where *TMP* is the transmembrane pressure, and μ is the permeate viscosity.

$$R_{ir} = \frac{TMP}{\mu \times J_{AF}} - R_m \qquad (6)$$

where J_{AF} is the water flux at 100 kPa after physical and chemical cleaning.

$$R_r = \frac{TMP}{\mu \times J_F} - R_m - R_{ir} \qquad (7)$$

where J_F is the humic acid filtration flux.

3. Results and Discussion

3.1 Exfoliation and characterisation of the boron nitride nanosheets

The ideal characteristics for 2D nanomaterial for use as fillers in a mixed matrix polymer membrane are relatively large lateral dimension (~1 μm), few layers as possible and, in the case of BNNS, retention of the sp^2 B-N bond structure. Exfoliation methods reported in the literature have primarily focused on producing single- or few-layer structures, involving long sonication times and at the expense of lateral size and yield [11-14]. Here a novel h-BN exfoliation method is used to produce boron nitride nanosheets (BNNS) of ~1 μm in diameter (Fig. 1a) with almost approximately equal distribution of B and N atoms (Fig. 1b,c) and a thickness of 5~6 nm (Fig. 1d), equivalent to about 15~18 layers [27]. This is the result of a gentler exfoliation process, consisting of successive ultrasonication and microwave irradiation steps, resulting in a more rapid exfoliation of relatively larger BNNS with reduced final BNNS thickness. Additionally, the protocol presented here preserves crystal structure of the BNNS, as confirmed by XRD (Fig. 1e), showing diffraction peaks corresponding to the (002), (100), (101), (102), (004), (110), and (112) planes of the hexagonal phase of BN, with lattice constants of a = 0.2504 nm and c = 0.6656 nm (JCPDS card 34-0421) [14]. The presence of BNNS is also confirmed by SAED pattern of the sample (Fig. S5). FT-IR spectrum of the sample (Fig. 1f) shows the vibration bands of ~3440 cm^{-1} (B-NH_2/B-OH), ~1660 cm^{-1} (N-H/CO), ~1370 cm^{-1} (in plane B-N transverse stretching), 1080 cm^{-1} (B-O-H/CO) and ~820 cm^{-1} (out-of-plane B-N-B bending) [18, 28, 29]. Raman spectroscopy (Fig. 1g) shows the characteristic peak centred at 1370 cm^{-1} ascribed to the high-frequency E_{2g} vibrational mode of *h*-BN [30]. The BNNSs produced after the exfoliation have similar XRD patterns and Raman peaks to that of *h*-BN, confirming the successful exfoliation process without generating measureable amounts of impurities. The FT-IR spectrum differs from that of *h*-BN powder (Fig. S5), showing the presence of B-NH_2 and B-OH groups on BNNS surface, which indicate hydrophilization of the structure, which is beneficial to their use in enhancing the water permeance of polymer membranes.

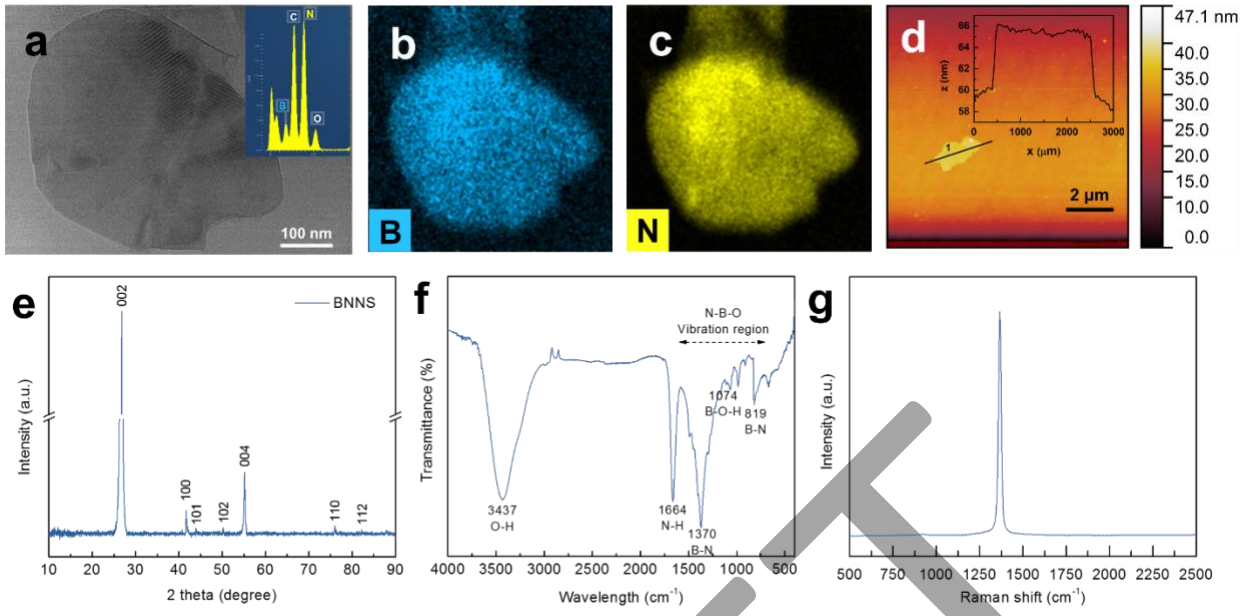

Fig. 1. Characterization of the produced BNNS: (a) TEM micrograph (inset: EDX spectrum); (b,c) EDS mapping of the same region; (d) AFM; (e) XRD, (f) FT-IR and (g) Raman spectra.

A schematic illustration of the exfoliation and preparation of BNNS as fillers is shown in Fig. 2. Sodium dodecyl sulfate (SDS) was used as the surfactant to (i) enhance the exfoliation of *h*-BN in Step A and (ii) improve its compatibility with the PES polymer in Step B [31, 32]. After exfoliation of *h*-BN to BNNS, a solvent exchange process was performed, yielding BNNS in NMP (Step B). The BNNS dispersion was continuously stirred, paying attention to avoid any drying of the dispersion. This was done to prevent the BNNSs from restacking before dispersing them in the polymer dope solution. NMP was added until the desired concentration of BNNS was reached. The BNNS dispersion was continuously stirred for several hours before PES resins were added, followed by a typical preparation of polymer dope solution for casting. Details of the procedure can be found in the experimental section.

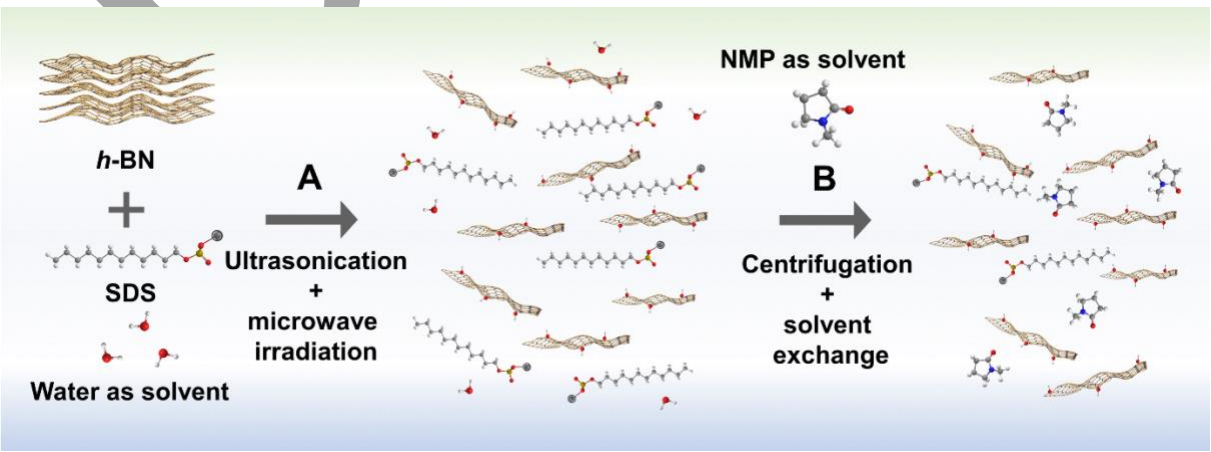

Fig. 2. Schematic illustration of the exfoliation of *h*-BN and preparation for its use as a filler.

3.2 Characterization of PES-BNNS membranes

The polymer membranes with different loadings of BNNSs (0.025, 0.05, and 0.1 wt%) were denoted as PBNS0.025, PBNS0.05 and PBNS0.1 (Table 1). SEM micrographs of the cross section of PBNS0.05 (Fig. 3a–c) show a typical finger-like microstructure extending to larger macrovoids from the top to the bottom of the membrane. The distribution of BNNS in the PBNS membranes was confirmed by Raman mapping (Fig. 3e) of the region highlighted in Fig. 3d of the cross-sectional SEM micrograph of PBNS0.1. The Raman map shows an even distribution of BNNS throughout the membrane cross-section, where the Raman intensity at 1370 cm^{-1} is denoted as red pixels. Variations in intensity are attributed to differences in the depth in different regions of the membrane, size or orientation of the BNNS (Fig. S6). The changes to the distribution with loading of BNNS are probed by Raman mapping of the surface of pure PES and PBNS membranes (Fig. 3f–l and Fig. S7). Here the characteristic Raman peak of BNNS at an intensity of 1370 cm^{-1} is denoted as green spots. As the loading of BNNS increases, more BNNSs are detected on the surface of the membrane. Furthermore, larger aggregates of BNNS are found on the surface of the membrane with higher loading of BNNS, suggesting a threshold loading of BNNS in PES membrane which, when exceeded, leads to aggregation. The surface morphologies of the membranes are shown in Fig. 3j –m.

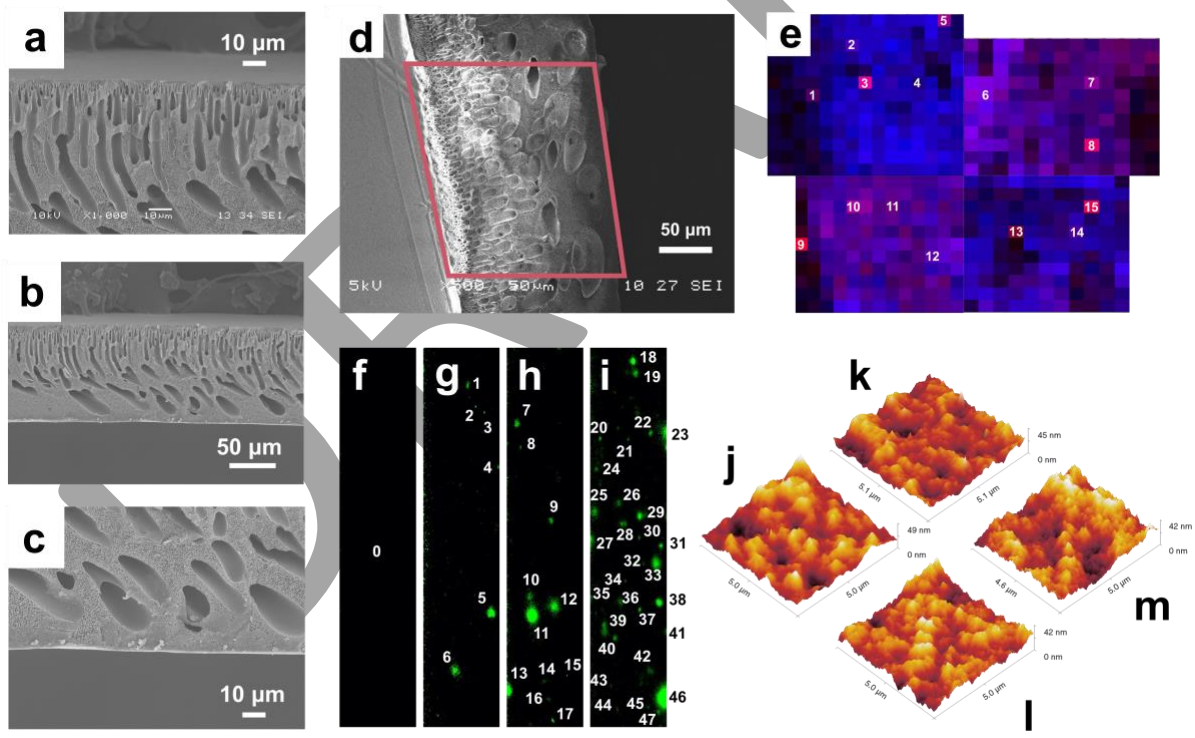

Fig. 3. Characterization of PBNS membranes: SEM micrographs of the cross-section of PBNS0.05 showing a) finger-like region, b) overview, and c) macrovoid region; d) overview of PBNS0.1; and e) Raman mapping of the highlighted region in d). The red pixels in (e) represents the location of BNNS while the blue pixel represents the PES polymer. Raman mapping and AFM of the surface of f,j) PES-pure, g,k) PBNS0.025, h,l) PBNS0.05, and i,m) PBNS0.1.

The surface roughness decreases with increasing BNNS loading from 0.025 to 0.5 wt%, while a further increase to 1.0 wt% results in higher roughness (Table 2). These changes can be ascribed to the effect of BNNS on the non-solvent induced phase separation during the formation of the membrane (Fig. 4). The decreased roughness will improve the anti-fouling properties of the membranes [33]. A similar trend is also observed for changes in the membrane cross section, where a BNNS loading beyond 0.05 wt% leads to a morphology resembling that of a pristine PES membrane (Fig. 4).

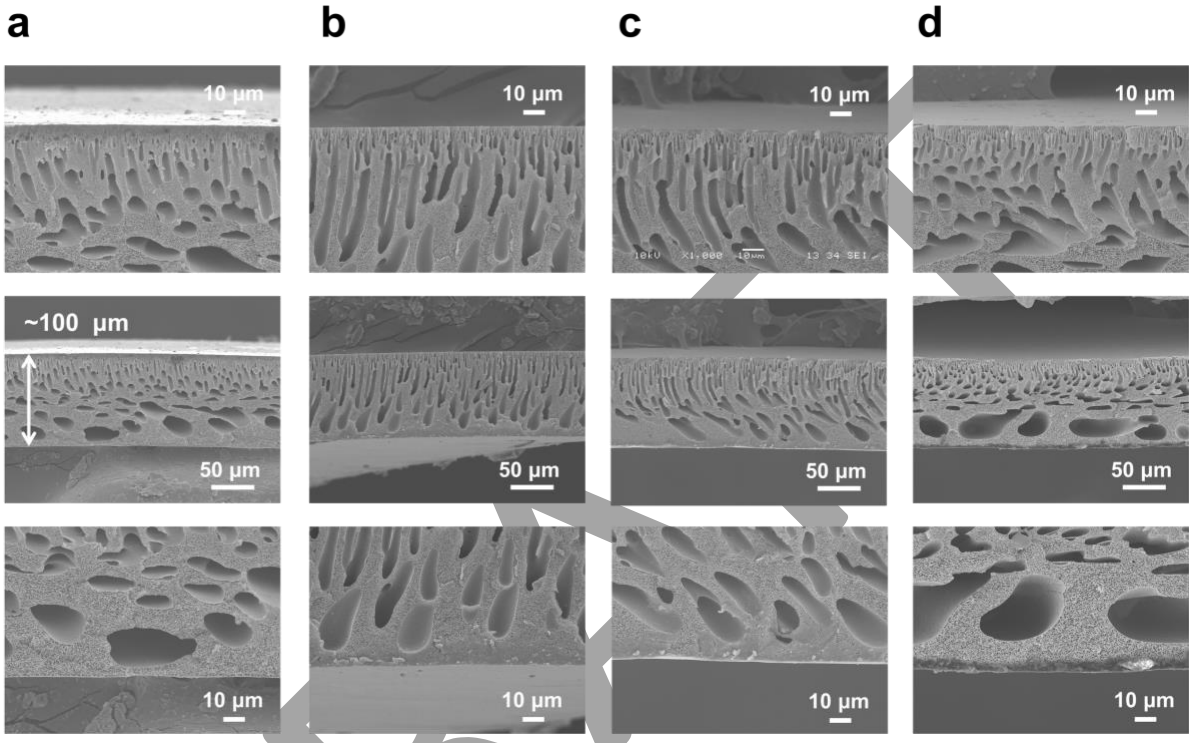

Fig. 4. Membrane cross section (a) Pure-PES, (b) PBNS0.025, (c) PBNS0.05, and (d) PBNS0.1.

Contact angle goniometry on the membrane surfaces shows that the water contact angle, polar force and surface free energy are increased, while the diiodomethane contact angle and dispersive force are decreased (Table 2). The increase in the hydrophilicity is due to the changes to the surface roughness and surface charge, whereby increasing loading of BNNS causes the surface of the membranes to become more negatively charged as determined from surface zeta potential measurement (Table 2). The overall porosities of the PBNS membranes are similar to the pristine PES membrane. The changes to the surface property of the membranes have significant impacts on the membrane performance, especially in terms of fouling resistance and water permeability.

Table 2. PBNS membrane surface properties.

Sample	Water contact angle (±2 °)	Diiodomethane contact angle (±2 °)	dispersive force (mJ/m²)	polar force (mJ/m²)	Surface free energy (mJ/m²)	Surface zeta potential (mV)	Surface average roughness, Sa (nm)	RMS height, Sq (nm)	Porosity (%)
PES-Pure	77	26	42	4.0	46 ± 1	-19.5 ± 3	6.0	7.4	52
PBNS0.025	57	31	35	16	51 ± 1	-35.7 ±3	4.9	6.2	49
PBNS0.05	56	28	36	16	52± 2	-43.8 ± 5	4.7	5.8	51
PBNS0.1	57	30	35	16	51± 2	-63.2 ± 4	5.7	7.0	50

3.3 Performance of PES-BNNS membrane

The performance of the PES-BNNS membranes was investigated in terms of pure water permeance, rejection of the dye Rose Bengal, and fouling by humic acid. Fig. 5 shows the comparison of membrane performance of PBNS and the pristine PES membrane. Initially, the addition of BNNS increases the water permeance while maintaining the comparable rejection of Rose Bengal. Beyond the optimal loading of 0.05 wt%, the water permeance decreases to the initial value which can be ascribed to the agglomeration of BNNS, as observed via Raman mapping (Fig. 3). Measurement of the concentration of Rose Bengal in feed, permeate and retentate showed, consistently, a mass balance > 98%, indicating that adsorption of the dye by the BNNS is minimal. The increase in permeance and decrease in rejection are attributed to a plasticizing effect of the BNNSs promoting the sliding of the polymer chains [34]. This is confirmed by the observation of a gradual decrease in the storage modulus (Fig. 5b) and the glass transition temperature of the membranes (Fig. S8) with increasing BNNS loading.

Fresh membranes were subjected to fouling test in cross-flow mode, whereby the membranes were first pre-compacted (at 1000 kPa), then their flux (at 800 kPa) was measured, and finally they were fouled with humic acid at 400 kPa for 4 h. After fouling, cleaning-in-place was performed for 1 h before water permeance measurements and a 2nd fouling cycle was performed on the same membrane. Fig. 5c shows that the rejection of humic acid is consistently above 97 % and 95% in the first and second cycle, respectively, indicating that most foulants are rejected by the membranes. The concentration of humic acid on the feed side of the membrane increased from 1% to ~30% at the end of the fouling cycle due to the rejection of humic acid and permeation of water across the membrane. Fig. 5d and 5e show the permeance and normalized permeance of the membranes, where the pure water permeance was measured in the first 60 min and during and after the cleaning cycle, while the permeance of the fouling solution was measured during the fouling stage. PBNS0.025 and PBNS0.05 clearly demonstrated excellent fouling resistance and flux recovery as shown by the consistently higher solution permeance than pure PES membrane and PBNS0.1 during the fouling stage and after the cleaning stage. Only ~80% water flux was recovered for the pure PES membrane while the PBNS membranes completely recovered or even exceeded the initial pure water permeance (Fig. 5e), with minimal irreversible fouling (Fig. 5f). We ascribe the latter result to the light de-compaction of the membranes observed during the cleaning cycle, performed at lower pressure than the compaction. PBNS0.1 showed the lowest solution permeance of the three PBNS membranes during the fouling cycle, and this is attributed to

the higher surface roughness, higher agglomeration rate and membrane cross-sectional structure resembling that of the pure PES membrane. However, PBNS0.1 still exhibits a complete flux recovery due to the addition of BNNSs which increase (in absolute terms) the overall zeta potential of the membrane.

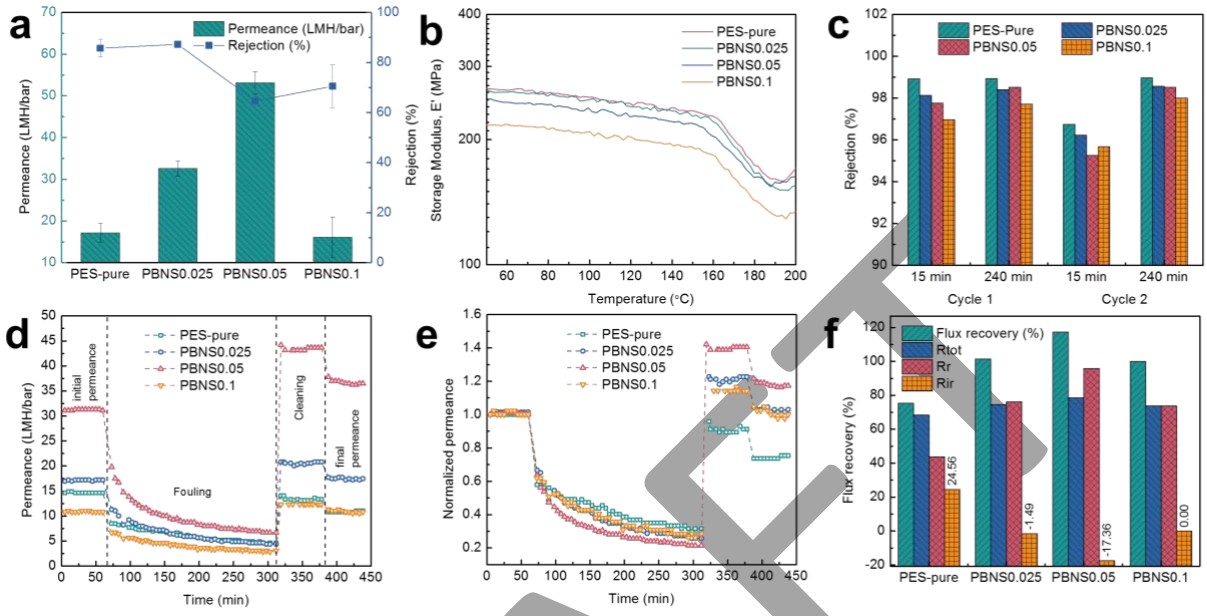

Fig. 5. PBNS membrane performance: a) Water permeance and Rose Bengal rejection, b) storage modulus, c) Humic acid rejection in the two fouling cycles, d) Fouling behavior in the first fouling and cleaning cycle, e) Normalized water permeance in the first fouling and cleaning cycle, and f) Flux recovery, total fouling ratio, reversible fouling ratio and irreversible fouling ratio of PBNS membrane in the first fouling experiment.

Excellent fouling resistance and water recovery were maintained after a second fouling cycle, with the membranes following a similar trend to the first cycle (Fig. 6a): PBNS0.025 and PBNS0.05 showed consistently higher solution permeance than pure PES and PBNS0.1, with high water permeance recovery obtained for all modified membranes. Since the water flux was not completely recovered for the pure PES membrane in the first fouling cycle, the second fouling experiment started with a lower initial water permeance of ~10 LMH/bar as opposed to 15 LMH/bar in the first cycle (Fig. 6b). All membranes exhibit high stability throughout the two fouling and cleaning cycles, without significant deviation for both the water permeance and solute rejection.

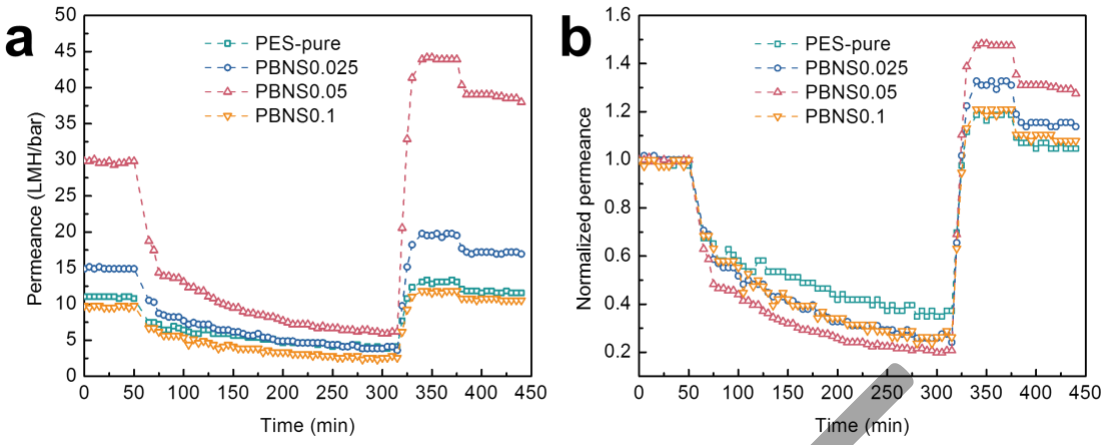

Fig. 6. Fouling behavior in the second fouling and cleaning cycle, e) Normalized water permeance in the second fouling and cleaning cycle.

4. Conclusions

Boron nitride nanosheet - PES mixed-matrix nanofiltration membranes have been successfully fabricated with high water permeance, fouling resistance and water flux recovery. The enhanced membrane performance was attributed to the improvement to the non-solvent induced phase separation process that produced porosity in the nanofiltration range suitable for high water permeance, and the modification of the surface properties of the membrane such as the surface roughness and surface charges that enhanced the fouling resistance and water flux recovery. The low amount of BNNS filler needed to render the mixed-matrix membrane fouling-resistant opens the way to its use in waste-water treatment applications, where fouling removal remains the main contributing factor to running costs of membrane-based plants.

Supporting Information

Supporting Information is available online.

Acknowledgements

The work is supported by EPSRC Programme Grant EP/M01486X/1 (SynFabFun) funded by the Engineering and Physical Sciences Research Council (EPSRC). The authors are grateful to Prof. Kang Li for providing us the PES resins, Dr. Philip Fletcher, Dr. Bo Wang, and Ms. Serena Casanova for their valuable discussions. The authors wish to dedicate this paper to their colleague, Dr Darrell Patterson.

References

[1] Y. Cui, S.I. Kundalwal, S. Kumar, Gas barrier performance of graphene/polymer nanocomposites, Carbon 98 (2016) 313-333.
[2] S. Zinadini, A.A. Zinatizadeh, M. Rahimi, V. Vatanpour, H. Zangeneh, Preparation of a novel antifouling mixed matrix PES membrane by embedding graphene oxide nanoplates, Journal of Membrane Science 453 (2014) 292-301.
[3] Y. Wang, R. Ou, H. Wang, T. Xu, Graphene oxide modified graphitic carbon nitride as a modifier for thin film composite forward osmosis membrane, Journal of Membrane Science 475 (2015) 281-289.
[4] K. Cao, Z. Jiang, X. Zhang, Y. Zhang, J. Zhao, R. Xing, S. Yang, C. Gao, F. Pan, Highly water-selective hybrid membrane by incorporating g-C3N4 nanosheets into polymer matrix, Journal of Membrane Science 490 (2015) 72-83.
[5] G. Liu, W. Jin, N. Xu, Two-Dimensional-Material Membranes: A New Family of High-Performance Separation Membranes, Angewandte Chemie International Edition 55(43) (2016) 13384-13397.
[6] J. Yin, J. Li, Y. Hang, J. Yu, G. Tai, X. Li, Z. Zhang, W. Guo, Boron Nitride Nanostructures: Fabrication, Functionalization and Applications, Small 12(22) (2016) 2942–2968.
[7] D. Golberg, Y. Bando, Y. Huang, T. Terao, M. Mitome, C.C. Tang, C.Y. Zhi, Boron Nitride Nanotubes and Nanosheets, Acs Nano 4(6) (2010) 2979-2993.
[8] D. Golberg, Y. Bando, C.C. Tang, C.Y. Zhi, Boron Nitride Nanotubes, Advanced Materials 19(18) (2007) 2413-2432.
[9] Y. Lin, J.W. Connell, Advances in 2D boron nitride nanostructures: nanosheets, nanoribbons, nanomeshes, and hybrids with graphene, Nanoscale 4(22) (2012) 6908-6939.
[10] X. Wang, C. Zhi, L. Li, H. Zeng, C. Li, M. Mitome, D. Golberg, Y. Bando, "Chemical Blowing" of Thin-Walled Bubbles: High-Throughput Fabrication of Large-Area, Few-Layered BN and Cx-BN Nanosheets, Advanced Materials 23(35) (2011) 4072-4076.
[11] K.-G. Zhou, N.-N. Mao, H.-X. Wang, Y. Peng, H.-L. Zhang, A Mixed-Solvent Strategy for Efficient Exfoliation of Inorganic Graphene Analogues, Angewandte Chemie International Edition 50(46) (2011) 10839-10842.
[12] Z. Wang, Z. Tang, Q. Xue, Y. Huang, Y. Huang, M. Zhu, Z. Pei, H. Li, H. Jiang, C. Fu, C. Zhi, Fabrication of Boron Nitride Nanosheets by Exfoliation, The Chemical Record 16(3) (2016) 1204-1215.
[13] C. Zhi, Y. Bando, C. Tang, H. Kuwahara, D. Golberg, Large-scale fabrication of boron nitride nanosheets and their utilization in polymeric composites with improved thermal and mechanical properties, Adv. Mater. 21(28) (2009) 2889-2893.
[14] M. Du, Y. Wu, X. Hao, A facile chemical exfoliation method to obtain large size boron nitride nanosheets, CrystEngComm 15(9) (2013) 1782-1786.
[15] Y. Wang, Z. Shi, J. Yin, Boron nitride nanosheets: large-scale exfoliation in methanesulfonic acid and their composites with polybenzimidazole, Journal of Materials Chemistry 21(30) (2011) 11371-11377.

[16] S. Yu, X. Wang, H. Pang, R. Zhang, W. Song, D. Fu, T. Hayat, X. Wang, Boron nitride-based materials for the removal of pollutants from aqueous solutions: A review, Chemical Engineering Journal 333 (2018) 343-360.
[17] Y. Xue, P. Dai, X. Jiang, X. Wang, C. Zhang, D. Tang, Q. Weng, X. Wang, A. Pakdel, C. Tang, Y. Bando, D. Golberg, Template-free synthesis of boron nitride foam-like porous monoliths and their high-end applications in water purification, Journal of Materials Chemistry A 4(4) (2016) 1469-1478.
[18] J. Li, X. Xiao, X. Xu, J. Lin, Y. Huang, Y. Xue, P. Jin, J. Zou, C. Tang, Activated boron nitride as an effective adsorbent for metal ions and organic pollutants, Sci Rep 3 (2013) 3208.
[19] J. Li, Y. Huang, Z. Liu, J. Zhang, X. Liu, H. Luo, Y. Ma, X. Xu, Y. Lu, J. Lin, J. Zou, C. Tang, Chemical activation of boron nitride fibers for improved cationic dye removal performance, Journal of Materials Chemistry A 3(15) (2015) 8185-8193.
[20] W. Lei, D. Portehault, D. Liu, S. Qin, Y. Chen, Porous boron nitride nanosheets for effective water cleaning, Nature communications 4 (2013) 1777.
[21] Y. Lin, T.V. Williams, T.-B. Xu, W. Cao, H.E. Elsayed-Ali, J.W. Connell, Aqueous Dispersions of Few-Layered and Monolayered Hexagonal Boron Nitride Nanosheets from Sonication-Assisted Hydrolysis: Critical Role of Water, The Journal of Physical Chemistry C 115(6) (2011) 2679-2685.
[22] Y. Yu, H. Chen, Y. Liu, V.S.J. Craig, C. Wang, L.H. Li, Y. Chen, Superhydrophobic and Superoleophilic Porous Boron Nitride Nanosheet/Polyvinylidene Fluoride Composite Material for Oil-Polluted Water Cleanup, Advanced Materials Interfaces 2(1) (2015) 1400267-n/a.
[23] D. Liu, L. He, W. Lei, K.D. Klika, L. Kong, Y. Chen, Multifunctional Polymer/Porous Boron Nitride Nanosheet Membranes for Superior Trapping Emulsified Oils and Organic Molecules, Advanced Materials Interfaces 2(12) (2015) 1500228-n/a.
[24] W. Meng, Y. Huang, Y. Fu, Z. Wang, C. Zhi, Polymer composites of boron nitride nanotubes and nanosheets, Journal of Materials Chemistry C 2(47) (2014) 10049-10061.
[25] W. Lei, V.N. Mochalin, D. Liu, S. Qin, Y. Gogotsi, Y. Chen, Boron nitride colloidal solutions, ultralight aerogels and freestanding membranes through one-step exfoliation and functionalization, Nature communications 6 (2015) 8849.
[26] D.K. Owens, R.C. Wendt, Estimation of the Surface Free Energy of Polymers, Journal of Applied Polymer Science 13 (1969) 1741-1747.
[27] J.C. Meyer, A. Chuvilin, G. Algara-Siller, J. Biskupek, U. Kaiser, Selective sputtering and atomic resolution imaging of atomically thin boron nitride membranes, Nano Lett. 9(7) (2009) 2683-2689.
[28] C. Tang, Y. Bando, Y. Huang, C. Zhi, D. Golberg, Synthetic Routes and Formation Mechanisms of Spherical Boron Nitride Nanoparticles, Advanced Functional Materials 18(22) (2008) 3653-3661.
[29] C. Huang, C. Chen, X. Ye, W. Ye, J. Hu, C. Xu, X. Qiu, Stable colloidal boron nitride nanosheet dispersion and its potential application in catalysis, Journal of Materials Chemistry A 1(39) (2013) 12192-12197.

[30] R. Arenal, A.C. Ferrari, S. Reich, L. Wirtz, J.Y. Mevellec, S. Lefrant, A. Rubio, A. Loiseau, Raman Spectroscopy of Single-Wall Boron Nitride Nanotubes, Nano Letters 6(8) (2006) 1812-1816.
[31] G. Wang, G. Olofsson, Titration Calorimetric Study of the Interaction between Ionic Surfactants and Uncharged Polymers in Aqueous Solution, The Journal of Physical Chemistry B 102(46) (1998) 9276-9283.
[32] W. Shihu, W. Wei, Y. Lingke, Z. Zhan, S. Daoheng, The fast fabrication of flexible electronic devices of graphene composites, Nanotechnology 27(31) (2016) 31LT01.
[33] M.N. Abu Seman, M. Khayet, Z.I. Bin Ali, N. Hilal, Reduction of nanofiltration membrane fouling by UV-initiated graft polymerization technique, Journal of Membrane Science 355(1) (2010) 133-141.
[34] K. Te Nijenhuis, H.H. Winter, Mechanical properties at the gel point of a crystallizing poly(vinyl chloride) solution, Macromolecules 22(1) (1989) 411-414.